INTERNATIONAL JOURNAL FOR NUMERICAL METHODS IN FLUIDS, VOL. 22, 449–465 (1996)

ACOUSTIC–MEAN FLOW INTERACTION AND VORTEX SHEDDING IN SOLID ROCKET MOTORS

A. KOURTA

Institut de Mécanique des Fluides de Toulouse, INPT, URA CNRS 0005, Avenue du Professeur Camille Soula, F-31400 Toulouse Cedex, France

and

Centre Européen de Recherche et de Formation Avancée en Calcul Scientifique (CERFACS), 42 Avenue G. Coriolis, F-31057 Toulouse Cedex, France

SUMMARY

The present work is devoted to the numerical simulation of two important phenomena in the field of solid propellant rocket motors: the first is acoustic boundary layers that develop above the burning propellant; the other is a periodic vortex-shedding phenomenon which is the result of a strong coupling between the instability of mean flow shear layers and acoustic motions in the chamber. To predict the acoustic boundary layer, computations were performed for the lower half of a rectangular chamber with bottom-side injection. The outflow pressure is sinusoidally perturbed at a given frequency. For the highest CFL numbers the implicit scheme is not able to compute the unsteadiness in the acoustic boundary layer. With very low CFL numbers or with the explicit scheme the main features of the acoustic field are captured. To simulate the vortex-shedding mechanism in a segmented solid rocket motor, the explicit version is used. This computation shows a mechanism for 'self-excited' vortex shedding close to the second axial mode frequency. The use of the flux-splitting technique reduces substantially the amplitude of the oscillations. A few iterations are done with flux splitting, then the computation is performed without this technique. In this case both the frequency and the intensity are well predicted. A geometry more representative of the solid rocket motor is also computed. In this case the vortex-shedding process is more complex and pairing is observed.

KEY WORDS: aeroacoustic; vortex shedding; solid rocket motor; implicit or explicit method

1. INTRODUCTION

This work is part of the overall combustion stability assessment of the Ariane 5 P230 MPS solid motor and has been supported by CNES within a research programme managed by ONERA. For this motor it is believed that there exists a severe risk of instability. The occurrence of low-amplitude but sustained oscillations pulsating at a frequency associated with one or more acoustic modes of the combustion cavity affects motor performances.[1–3] The unsteady or acoustic boundary layer that develops above the burning propellant appears to be an important feature of rocket motor stability. Such boundary layers are responsible for flow-turning losses[4,5] and govern the local unsteadiness of the flow. The burning propellant acts as the source of energy driving acoustic mode excitation. Instability occurs when the energy supplied by the combustion process excites one or more of the natural modes of the combustor.[6] This driving by the solid propellant combustion depends upon the space evolution of flow oscillation near the propellant surface. Hence it can be pressure or velocity coupling. An

CCC 0271-2091/96/060449-17

Received November 1994

approximation of the oscillation frequency is obtained by using the equation of resonance[7] $f = na/2L$ for a closed–closed cavity or $f = (2n - 1)a/4L$ for a closed–open cavity.

An additional mechanism that drives pressure oscillations in rocket motors is vortex shedding.[1,8] This vortex shedding can interact with the chamber acoustics to generate pressure oscillations.[9,10] Owing to the segmented design of solid propellant rocket motors, shear layers induced by surface discontinuities appear and can produce vortex shedding. The dipole mechanism involving the interaction of vortices with an impingement surface is one way that energy passes from the vortex fluctuations to the acoustic field. The interaction between vortices and an impingement surface causes fluctuating forces on the surface. Acoustically, the fluctuating force is equivalent to a dipole.[11] The energy transfer depends on the distance between the separation point and the impingement surface.[7] There are locations relative to the mode shape which are preferred for amplification.[12,13] Also, the presence of amplifying shear layers and reflecting surfaces can produce resonant acoustic energy flows into frequencies governed by the resonance condition produced by a non-linear quadratic interaction between the various modes of oscillation.[3] In the rocket motor the vortex shedding is periodic.[2,8] It is the result of a strong coupling between the instability of mean shear flow and the organ-pipe acoustic mode in the chamber. The feedback from the acoustic wave provides the control signal for the hydrodynamic instability. In the presence of an acoustic wave in the correct frequency range a strong correlative signal is present which organizes the vortical disturbance. Moreover, significant increases in acoustic pressure amplitude can be generated by coupling from periodic vortex shedding.[12] Examples of cases where the unstable separated flows can couple with the acoustics to produce a significant source of energy are the cavity tone, edge tone, hole tone and ring tone. The internal configuration of segmented solid propellant motors can present one or often more of these couplings. The shedding frequency of periodic vortex flows can be characterized by the Strouhal number[1,7,12] $S = fl/u$, where u is the velocity on the centreline and l is the characteristic length (it can be the transverse dimension of the disturbing body or the length between resistor pairs).

Acoustic mode excitation can be predicted by linearized acoustic instability models.[1,4,14] The stability analysis of a motor is often equivalent to determining whether the acoustic modes grow or decay. Predictions of stability are made by identification of both the acoustic energy gains and losses in the motor.[5] Two different models have been developed to predict the acoustic oscillation in a motor:[4,5] the flow-turning and admittance correction approaches. The flow-turning approach (one- or multidimensional analysis) has been widely used because of its relative simplicity, although the admittance correction approach seems more rigorous. Comparison between these two methods and experimental results shows better prediction with the admittance correction model.[4] These stability models are based on a quasi-incompressible mean flow field assumption. Thus the choked ejection nozzle is not concerned by this analysis. The aft-end plane has to be located within the low-Mach-number domain. Also, in the rocket motor the initial region of linear spatial growth, where the unstable shear layer is amplified and periodic shedding of vortices is observed, is followed by a zone of complex non-linear interaction in which vortex pairing may take place.

Because of the complexity of the problem, an analytical solution to the governing equations with complex boundary conditions is not possible. Numerical simulations, if performed properly, may provide important help in understanding the complex physics. Numerical simulations of unsteady compressible flow have been developed.[11,15,16] Such simulations should naturally couple mean flow shear layer and acoustic motions. Numerical methods have been performed to isolate and study the interaction between acoustic waves and vortex structures. This interaction has been studied in an axisymmetric ramjet combustor.[16–18] Vuillot and Avalon[19] and Lupoglazoff and Vuillot[20] used the MacCormack explicit scheme with artificial viscosity to compute the acoustic–mean flow interaction.

The present work is also concerned with numerical simulation. The aim of this paper is to present the ability of numerical codes to predict the unsteady behaviour inside the combustion chambers of solid propellant rocket motors. For this kind of computation the numerical methods must have good properties: good accuracy and stability, little artificial dissipation and small time consumption. Also, the scheme has to be non-dissipative and non-dispersive.[21] Thus in this paper the dissipative and dispersive errors will be examined. The numerical method is a version of the explicit–implicit MacCormack method. To avoid the use of artificial viscosity, a flux-splitting technique can be used. Three test cases will be presented in this paper and different numerical options of the scheme will be tested.

The first test case concerns an acoustic boundary layer simulation. Two-dimensional (2D) computations were performed for the lower half of a rectangular chamber with bottom-side injection. Before performing the unsteady calculation, an initial condition corresponding to a steady state solution is obtained by using an implicit version of the numerical scheme. Starting from this steady solution, the unsteady calculation was done.

The second test case is devoted to the vortex-shedding phenomenon inside a 2D test case solid propellant motor. In this part only the explicit version is used. The computations show the ability of the code to simulate the vortex shedding and to predict the coupling between the instability of the mean flow shear layers and the acoustic motion.

The last case concerns a more realistic solid rocket motor geometry. The configuration is axisymmetric and the multiblock technique is used.

2. METHODOLOGY

2.1. Governing equations

The physical model used involves the full Navier–Stokes equations. This model describes the conservation of mass, momentum and total energy. These equations can be written in vector form as

$$\frac{\partial W}{\partial t}+\frac{\partial F}{\partial x}+\frac{1}{r^k}\frac{\partial (r^k G)}{\partial r}=H, \tag{1}$$

$$W=\begin{bmatrix}\rho\\ \rho U\\ \rho V\\ \rho E\end{bmatrix},\qquad f=\begin{bmatrix}\rho U\\ \rho U^2+\sigma_{xx}\\ \rho UV+\sigma_{xr}\\ (\rho E+\sigma_{xx})U+\sigma_{xr}V-\lambda\partial T/\partial x\end{bmatrix},$$

$$G=\begin{bmatrix}\rho V\\ \rho UV+\sigma_{rx}\\ \rho V^2+\sigma_{rr}\\ (\rho E+\sigma_{rr})V+\sigma_{rx}U-\lambda\partial T/\partial r\end{bmatrix},\qquad H=\begin{bmatrix}0\\ 0\\ (k/r)(P+\sigma_{\theta\theta})\\ 0\end{bmatrix},$$

with

$$k=\begin{cases}1, & \text{axisymmetric}\\ 0, & \text{2D,}\end{cases}$$

$$\sigma_{xx}=P-\mu\left[2\frac{\partial U}{\partial x}-\frac{2}{3}\left(\frac{\partial U}{\partial x}+\frac{1}{r^k}\frac{\partial r^k V}{\partial r}\right)\right],\qquad \sigma_{xr}=\sigma_{rx}=-\mu\left(\frac{\partial U}{\partial r}+\frac{\partial V}{\partial x}\right),$$

$$\sigma_{rr}=P-\mu\left[2\frac{\partial V}{\partial r}-\frac{2}{3}\left(\frac{\partial U}{\partial x}+\frac{1}{r^k}\frac{\partial r^k V}{\partial r}\right)\right],\qquad \sigma_{\theta\theta}=-k\mu\left[2\frac{V}{r}-\frac{2}{3}\left(\frac{\partial U}{\partial x}+\frac{1}{r}\frac{\partial rV}{\partial r}\right)\right].$$

To close this set of equations, the pressure is related to the other state variables ρ and T by the law of state for perfect gases.

2.2. *Numerical method*

The numerical method is a version of the explicit–implicit MacCormack scheme.[22,23] It consists of a predictor–corrector approach. For each time step an explicit increment is evaluated using forward or backward approximations for the inviscid part and central differences for the viscous terms. To remove the severe explicit stability restriction, this increment is updated with an implicit approximation of its evolution equation. This equation is obtained by taking the time derivative of the original motion equation:

$$\frac{\partial}{\partial t}\left(\frac{\partial W}{\partial t}\right)+\frac{\partial}{\partial t}\left(\frac{\partial F}{\partial x}\right)+\frac{\partial}{\partial t}\left(\frac{1}{r^k}\frac{\partial r^k G}{\partial r}\right)=\frac{\partial H}{\partial t}. \tag{2}$$

The implicit approximation can be written as

$$\left(I+\Delta t\frac{\partial A\bullet}{\partial x}+\Delta t\frac{1}{r^k}\frac{\partial r^k B\bullet}{\partial r}-\Delta t C\right)\delta W=\Delta W, \tag{3}$$

with the implicit and explicit increments written respectively as

$$\delta W=\frac{\partial W^{n+1}}{\partial t}\Delta t, \qquad \Delta W=\frac{\partial W^{n}}{\partial t}\Delta t.$$

In the previous equations the Jacobian matrices $A=\delta F/\delta W$ and $B=\delta G/\delta W$ include inviscid and viscous contributions.

Finally, the two steps of the scheme can be written as follows: for the predictor step,

$$\Delta W^{(n)}=-\Delta t\left(\frac{\partial F^{(n)}}{\partial x}+\frac{1}{r^k}\frac{\partial r^k G^{(n)}}{\partial r}-H\right),$$

$$\left[I+\Delta t\left(\frac{\partial A\bullet}{\partial x}+\frac{1}{r^k}\frac{\partial r^k B\bullet}{\partial r}-C\right)\right]\delta W^{(\overline{n+1})}=\Delta W^{(n)},$$

$$W^{(\overline{n+1})}=W^{(n)}+\delta W^{(\overline{n+1})};$$

for the corrector step,

$$\Delta W^{(n+1)}=-\Delta t\left(\frac{\partial F^{(\overline{n+1})}}{\partial x}+\frac{1}{r^k}\frac{\partial r^k G^{(\overline{n+1})}}{\partial r}-H\right),$$

$$\left[I+\Delta t\left(\frac{\partial A\bullet}{\partial x}+\frac{1}{r^k}\frac{\partial r^k B\bullet}{\partial r}-C\right)\right]\delta W^{(n+1)}=\Delta W^{(n+1)},$$

$$W^{(n+1)}=\tfrac{1}{2}\left(W^{(n)}+W^{(\overline{n+1})}+\delta W^{(n+1)}\right).$$

In order to improve the numerical efficiency, various ingredients have been included in the method. The most significant are the second-order-accurate flux splitting and a Gauss–Seidel line relaxation technique. The use of the flux-splitting technique was motivated by the need for a better description of discontinuities and a more rigourous treatment of the boundary conditions.[23] The flux splitting used here is close to the one developed by Steger and Warming.[23,24] It has the desirable property of enforcing the diagonally dominant character of the implicit matrix operator. Furthermore, the Gauss–Seidel line relaxation method avoids the use of approximate factorization and allows the use of unbounded CFL numbers.

2.3. *Computational domains*

In this paper three different configurations are computed. Figure 1a presents the first one (case I). The geometry is the lower half of a rectangular chamber with a blowing surface at the lower wall ($h = 20$ mm, $L = 581$ mm). The upper boundary is a plane of symmetry. The left side (head end) is a

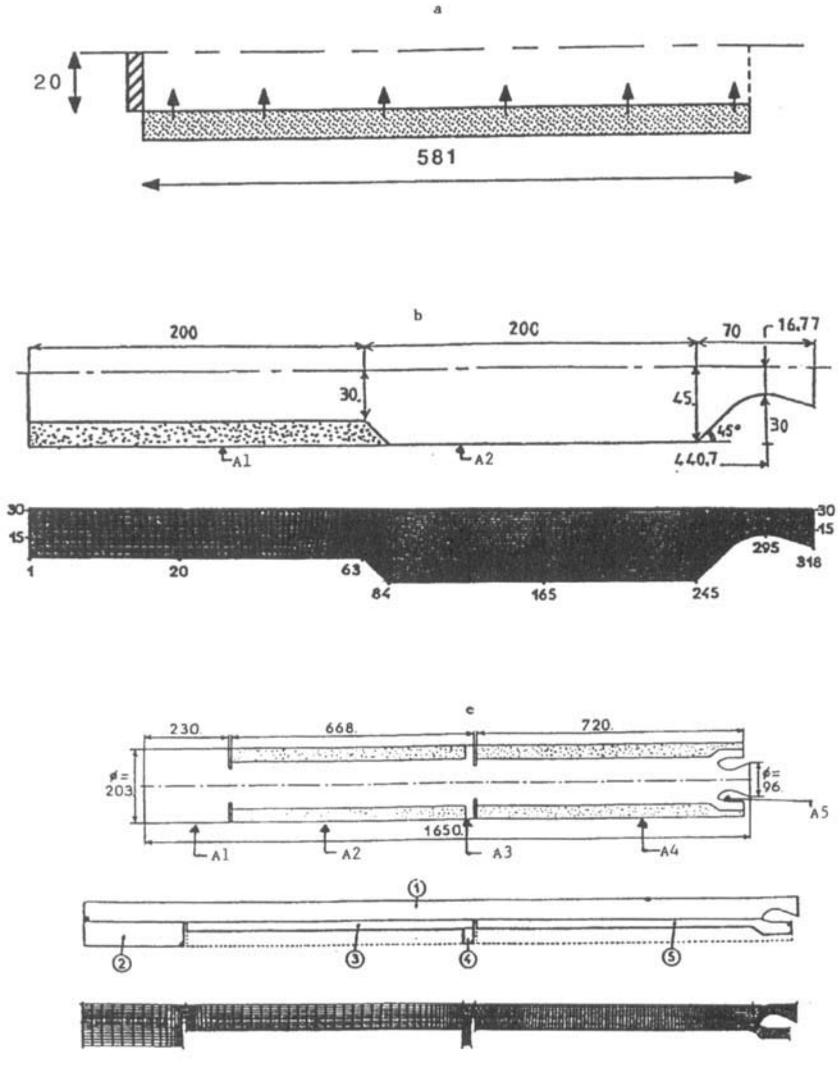

Figure 1. Computational domains: a, case I; b, case II; c, case III

rigid wall and the outflow boundary is at the right side. The mesh used (100 × 50) is characterized by a longitudinally uniform partition ($\Delta x = L/99$) and a stretched one in the lateral direction ($\Delta y_j = 1{\cdot}05026 \Delta y_{j-1}$, with $\Delta y_0 = 0{\cdot}1$ mm).

The second computational configuration (case II) is presented in Figure 1b. The grid is the same as the one used by Lupoglazoff and Vuillot.[20] This test case involves a sheared flow at the right-hand-side corner of the propellant grain. The length of the chamber was chosen in such a way that the first mode frequency was close to the critical frequency of the shear layer ($f_{cr} = 1320$ Hz). The length of this plane motor is 0·47 m with 0·2 m length grain.

The last test case computed (case III) is based on a segmented motor model. This case is axisymmetric and required a multiblock technique. It represents configuration A of the ONERA LP3 experiment. The chosen sequence corresponds to 20 mm of burning propellant, where an important instability at the third mode (900 Hz) was observed. The calculation was done with a coarse mesh (3000 points). The geometry and the mesh was presented in Figure 1c. The configuration is divided into five blocks.

2.4. *Boundary and initial conditions*

The boundary conditions imposed for the three computations are given in Table I. A1–A5 in this table are defined Figure 1.

The no-slip condition is imposed at the inert wall where the velocity and normal pressure gradient are equal to zero. At the injecting wall the mass flow rate, the temperature and zero tangential velocity are specified. For subsonic outflow the static pressure is fixed. For case I the static pressure value simulates a nozzle with an inlet-to-throat area ratio of five. In the case of supersonic outflow, classical first-order extrapolations are used.

For initial conditions the three computations are started from rest.

2.5. *Physical values*

Table II presents the physical values for case I. For the vortex-shedding cases the values used are given in Table III.

2.6. *Numerical parameters and performances*

Acoustic boundary layer case. For this case we compute first a steady solution with the implicit scheme and then the unsteady solution with both implicit and explicit schemes. The CPU times used for these different computations are given in Table IV.

For the unsteady case the implicit option has been tested with three different CFL numbers (Table V). Each one corresponds to a different number of iterations per period.

Table I. Boundary conditions

Case	Head end	Aft end	Internal side	External side
I	No slip	Subsonic outflow	Symmetry	Injecting wall
II	No slip	Supersonic outflow	Symmetry	A1: injecting wall A2: no-slip condition
III	No-slip	Supersonic outflow	Symmetry	A2, A4: injecting wall A1, A3, A5: no-slip condition

Table II. Physical values for case I (SI units)

R	γ	$\dot{m}$	T_i	μ	Pr	a
286·7	1·4	2·42	303	$1{\cdot}9 \times 10^{-5}$	1	348·7

Table III. Physical values for cases II and III (SI units)

Case	ρ_p	V_c	$\dot{m}$	T_f	a	R	μ	γ	Pr
II	1633	13×10^{-3}	21·201	3387	1075·43	299·53	36×10^{-5}	1·14	1
III	1640	$7{\cdot}38 \times 10^{-3}$	12·1032	2700	1061·27	340·53	$8{\cdot}1 \times 10^{-5}$	1·225	1

Table IV. CPU time and machine used

Case	Scheme	Number of iterations	CPU time (s)	Machine
Steady	Implicit	900	27900	Convex C220
Steady	Implicit	900	39600	Alliant FX80
Unsteady	Implicit	50/period	2200/period	Alliant FX80
Unsteady	Implicit	200/period	8800/period	Alliant FX80
Unsteady	Implicit	500/period	22000/period	Alliant FX80
Unsteady	Explicit	20000/period	28000/period	Alliant FX80

Table V. Different CFL numbers used

CFL number	460	115	46
Iterations/period	50	200	500

2D vortex-shedding case. For this test case calculation only the explicit version is used with or without the flux-splitting technique. The time step is $dt = 1{\cdot}623 \times 10^{-7}$ s and 350,000 iterations have been performed. The computation was done on a Convex C220 computer and for one time step 0·9 CPU second is needed.

Axisymmetric vortex-shedding case. This case is computed with the explicit version and without the flux-splitting technique. For the mesh used, the time step is $dt = 0{\cdot}5 \times 10^{-7}$ s and 300,000 iterations have been performed. For one time step 0·48 CPU second is needed on the Convex C220.

3. RESULTS

3.1. Acoustic boundary layer

This test case was defined in order to evaluate the ability of the numerical scheme to simulate the effect of periodic oscillations on an injected boundary layer.

Before performing unsteady computations, a steady solution has been evaluated. The computation is started from rest with the outlet pressure equal to $1{\cdot}5 \times 10^5$ Pa.

The steady solution has been reached after 900 iterations with the implicit version of the code. The steady state is shown in Figure 2. The maximum Mach number obtained inside the chamber is 0·1787.

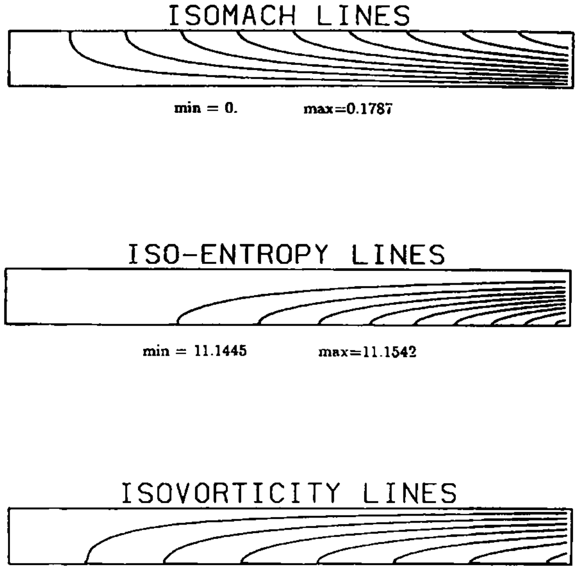

Figure 2. Steady acoustic boundary layer

This solution is very close to the analytical one obtained in the incompressible case. The well-known cosine velocity profiles for the 2D planar chamber are obtained.[25–27]

The previous steady solution is now used as an initial condition for the unsteady computation. The outflow static pressure is sinusoidally perturbed around its steady state value: $P'_s = P_s\{1 + \alpha \sin[2\pi f(t - t_0)]\}$, where $\alpha = 0{\cdot}01$ and $f = 343$ Hz. This forcing frequency has been chosen close to the first acoustic mode frequency ($f = 1{\cdot}143a/2L = 0{\cdot}5715a/L$) in order to have an acoustic pressure node inside the chamber.

This case was computed with both explicit and implicit versions. We present first the results obtained with the explicit version, then we discuss the effect of using an implicit scheme to compute unsteady flow.

The unsteady phase has been computed with the explicit version over 45 ms, corresponding to 15 periods of the forced oscillating pressure. A periodic regime is reached after 25 ms (eight periods). The evolutions of the velocity components U and V at different positions of the mid-chamber are plotted in Figure 3. For the U-component the mean value increases with the lateral position. The amplitude of the oscillation is maximum at a distance from the injection wall equal to 1·87 mm ($r/L = 3{\cdot}22 \times 10^{-3}$).

Figure 4 shows the amplitude and phase partition of the centreplane acoustic pressure and longitudinal velocity. A pressure node is located at $x/L = 0{\cdot}442$. The transverse profiles of longitudinal velocity at different longitudinal positions are presented in Figure 5. These velocity profiles indicate that an unsteady shear wave is created by unsteady viscous forces and propagates away from the injecting wall. These evolutions are in good agreement with the analytical ones.[4,19,28] The scheme is able to capture approximately all the overshoots predicted by the analytical method. It is indicated that a damping due to the numerical viscosity does not affect the solution. When a coarse mesh is used, the last overshoot is not predicted.[19] The same problem occurs when the scheme is too dissipative (Van Leer flux splitting).[29]

The implicit scheme allows minimization of the CPU times (Table IV). For this reason the implicit scheme is used to compute the unsteady case. The following tests were performed in order to evaluate the CFL number effects.

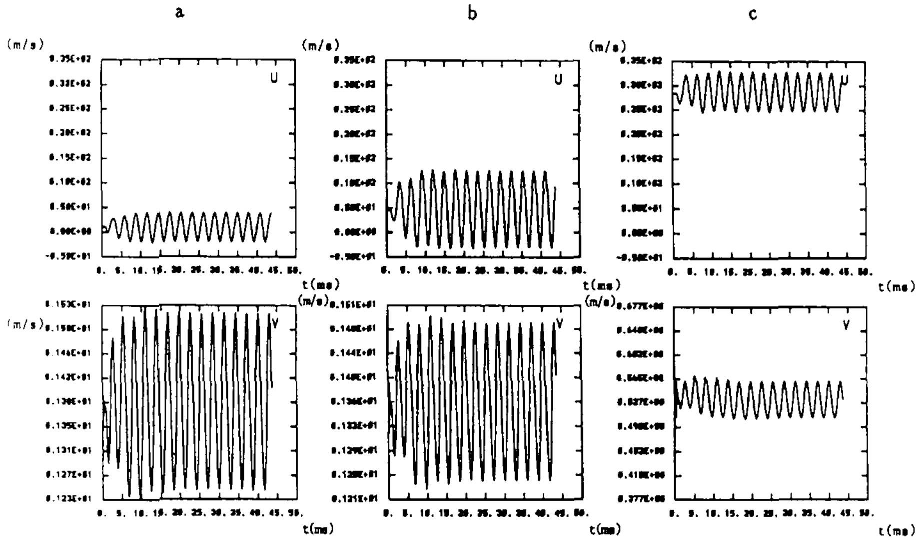

Figure 3. Time histories of velocity components for case I ($x/L=0{\cdot}5$): a, $r/L=6{\cdot}45\times10^{-4}$; b, $r/L=3{\cdot}22\times10^{-3}$; c, $r/L=25{\cdot}5\times10^{-3}$

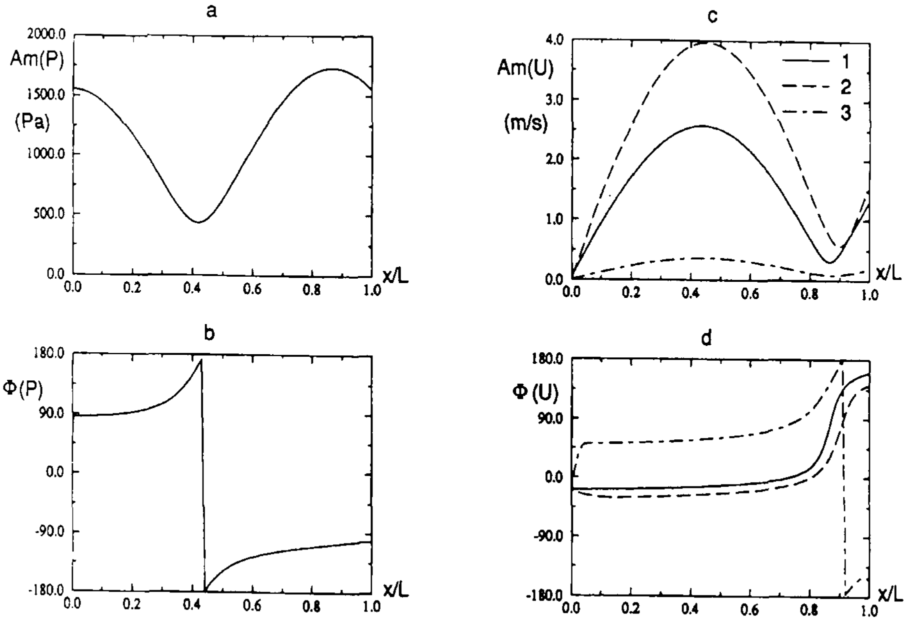

Figure 4. Centreplane acoustic pressure and axial velocity for case I: a, c, amplitude; b, d, phase (1, $r/L=39{\cdot}7\times10^{-3}$; 2, $r/L=10^{-2}$; 3, $r/L=8{\cdot}6\times10^{-5}$)

Figure 6 shows the head-end static pressure obtained with the different CFL values. For the three CFL numbers used, an unsteady phenomenon is predicted. However, for the higher value (460) an important damping of the signal amplitude is observed. When the CFL number decreases, this damping decreases. For the lower value of CFL number (46) the amplitude is approximately correct and the results are the same as those obtained with the explicit version. The consequence of this damping due to large CFL number is poor prediction of the position of the pressure node in the

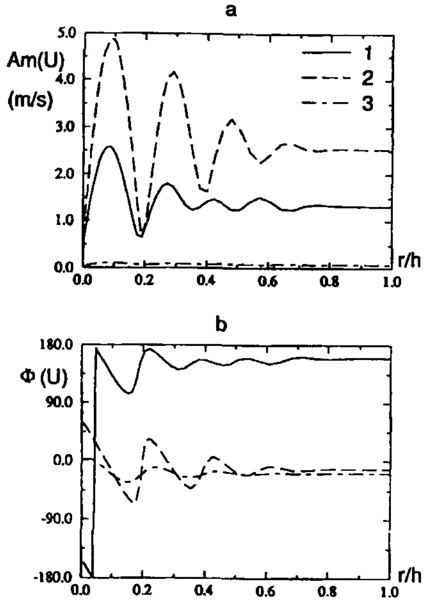

Figure 5. Transverse profiles of acoustic velocity for case I: a, amplitude; b, phase (1, $x/L = 99{\cdot}5 \times 10^{-2}$; 2, $x/L = 48 \times 10^{-2}$; 3, $x/L = 5 \times 10^{-3}$)

chamber and hence bad prediction of the acoustic boundary layer. From these calculations we can conclude that with higher CFL numbers the implicit scheme is very dissipative and leads to an important damping. Hence for very large CFL numbers even the unsteadiness cannot be observed. Thus is is clear that we have to restrict ourselves to low CFL numbers ($\leqslant 50$). However, owing to the relative CPU cost of each method and considering that the level of accuracy of both methods is equivalent, in this case it is better to use an explicit version in as far as we are concerned with the unsteadiness.

3.2. Vortex Shedding

The two test cases here are concerned with simulation and analysis of the vortex-shedding mechanism in the solid propellant rocket motor. The first case is a simple two-dimensional configuration. The goal of this computation is the capture of the vortex shedding. The velocity and pressure signals obtained at different positions in the flow illustrate the unsteady organized character of the flow.[30,31] The head-end pressure is shown in Figure 7. A periodic regime is reached after 28 ms. Figure 8 presents examples of the pressure and velocity time histories. The corresponding spectra are also reported. These spectra show a monochromatic character of the signal with a high peak at 2570 Hz. This frequency is close to the second axial mode frequency. Lupoglazoff and Vuillot[20] obtained the same periodic mechanism at a frequency equal to 2540 Hz. A comparison with their results has been made and the agreement is good. The coupling procedure is very sensitive to the position of the shear layer origin (X_0). Lupoglazoff and Vuillot,[20] using Flandro's method, show that for $241 \leqslant X_0 \leqslant 285$ mm, mode $2L$ should be unstable while mode $1L$ should be stable. This is in agreement with the numerical simulation results, because in this case X_0 is in this range.

For this case we did the computation with and without the flux-splitting technique. Some important differences appear and will be analysed. A damping effect is introduced when the flux-splitting technique is used. Table VI gives the head-end pressure and thrust obtained for these two cases. The

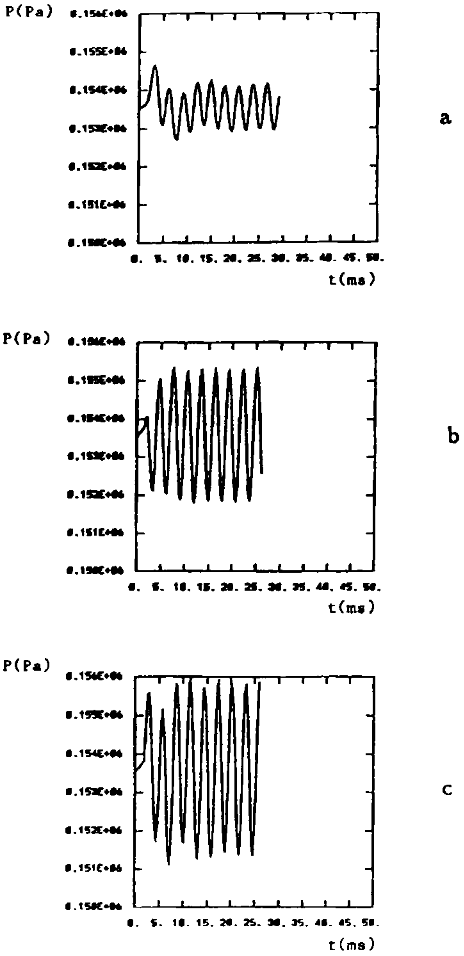

Figure 6. Time histories of head-end static pressure for case I: a, CFL = 460; b, CFL = 115; c, CFL = 46

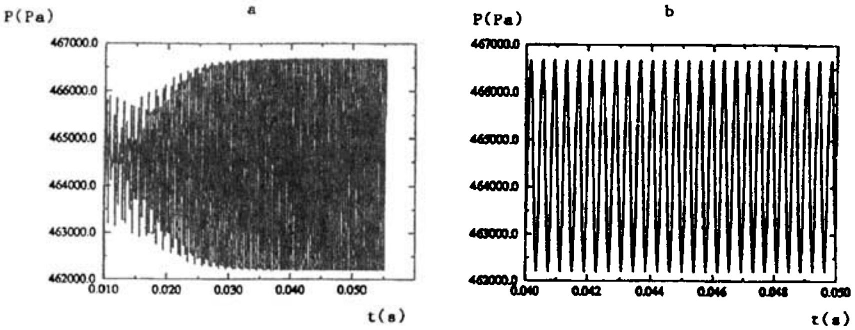

Figure 7. Time history of head-end static pressure for case II: a, complete history; b, 'zoom-in' ensemble

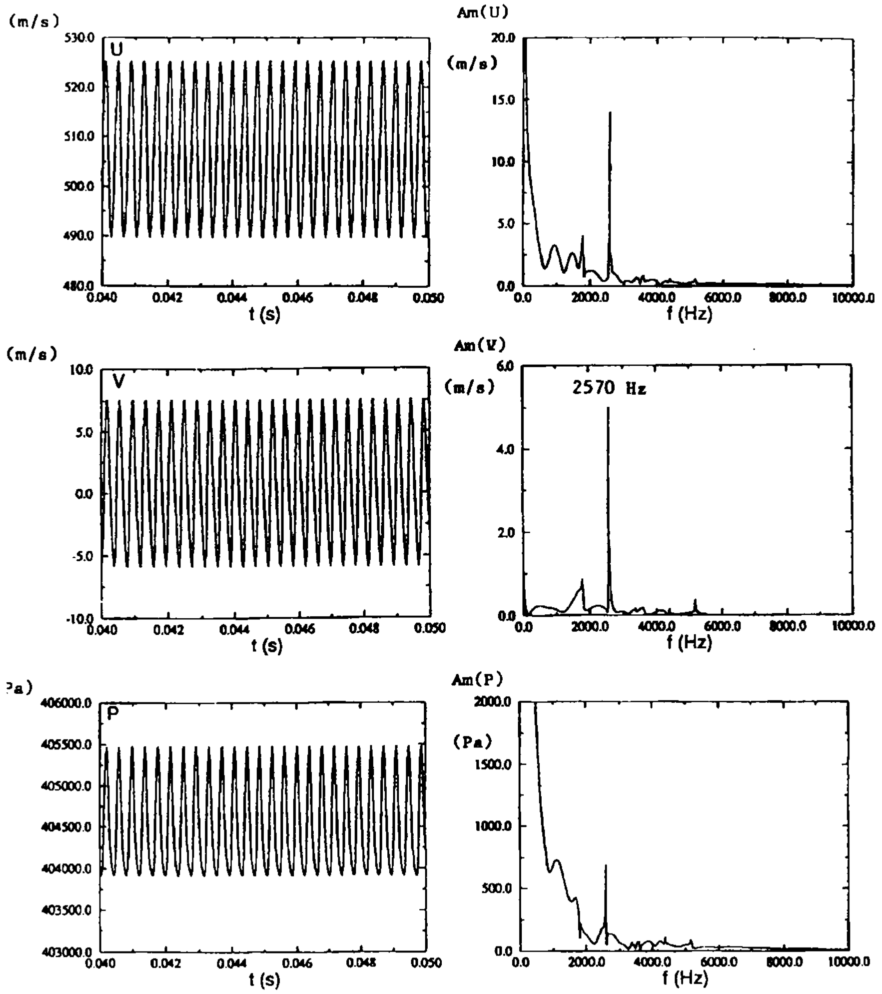

Figure 8. Time histories and spectra of velocity and pressure for case II ($x/L=0{\cdot}7835$, $r/L=0{\cdot}0867$)

mean values are slightly different. An important difference appears for the amplitude of the fluctuations.

Figure 9 presents the isovorticity contours obtained with and without flux splitting during one period ($f=2570$ Hz). In the mixing layer, coupled with acoustic oscillations, a periodic vortex shedding occurs. The interaction process can be quite complex; its essential mechanism may be described in the following simple manner. A shear flow is produced at the downstream end of the grain. Because the

Table VI. Pressure and thrust

	ΔP (Pa)	$\bar{P}$ (Pa)	ΔTh (N)	$\overline{Th}$ (N)
With flux splitting	4655	$0{\cdot}464 \times 10^6$	456	$0{\cdot}199 \times 10^5$
Without flux splitting	6379	$0{\cdot}466 \times 10^6$	530	$0{\cdot}202 \times 10^5$

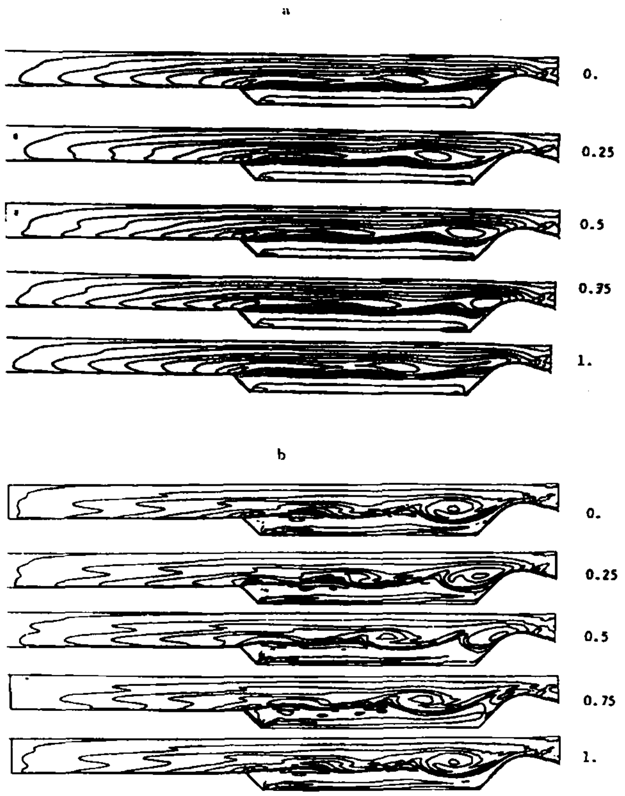

Figure 9. Isovorticity contours during one period ($f=2570$ Hz): a, with flux splitting; b, without flux splitting

velocity gradient is sufficiently large, this shear layer is unstable and small disturbances in the vicinity of the origin are spatially amplified, forming vortex structures. These vortices translate in the axial direction. A vortex impinging on the nozzle generates an acoustic disturbance. This acoustic disturbance propagates upstream and perturbs the shear layer origin. The consequence is the formation of vortical structures. The process is thus self-sustaining.

The flux-splitting effect can be observed in Figure 9. The isolines are irregular without this technique and are smoothed when it is introduced. To make the computation without flux splitting possible in this case, we start by using this technique to obtain an initial solution. Few iterations are needed (2000 iterations). With this solution we continue the calculation without flux splitting, which turns out to be necessary only for the transient period. This procedure will be adopted for computing the unsteady case with this code.

The test case computed is based on a segmented motor model and represents configuration A of the ONERA LP3 experiment.

Figure 10 shows the iso-entropy and velocity field at different times. It can be clearly observed that even this coarse mesh the vortex shedding is captured. The formation of the vortex can be seen and a pairing mechanism takes place. The new vortex resulting from the pairing mechanism is absorbed by the nozzle. The vortex mechanism is more complex than in the previous case. In the present case, different vortices with different sizes exist in the flow and complex non-linear interactions can appear. The signals obtained are not monochromatic and contain complex physical phenomena. Figure 11 presents the time evolution of the thrust. The velocity and pressure spectra confirm this complexity. In

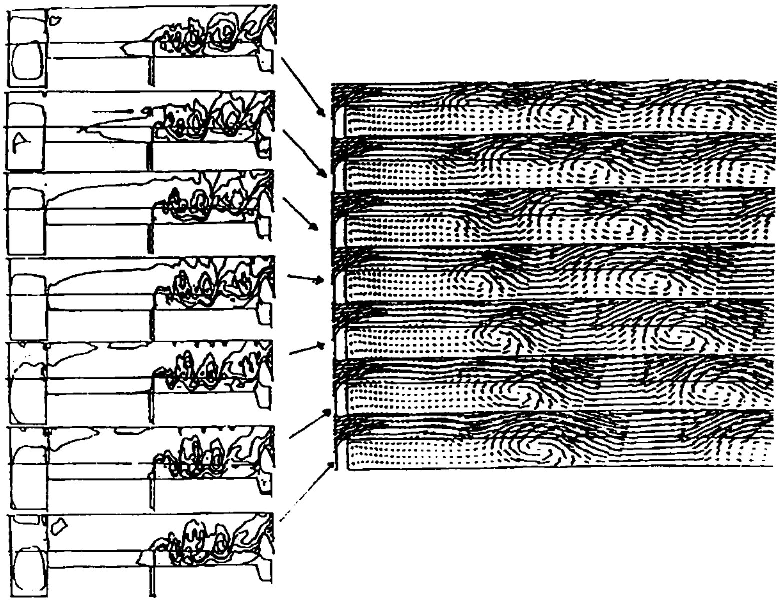

Figure 10. Iso-entropy and velocity field at different time stations for case III

fact, the spectra exhibit many peaks, as can be observed in Figure 12. The axial evolution of the spectra provides information on the non-linear vortex interaction. Near the shear layer origin, three dominant peaks (600, 1200 and 1800 Hz) are present (Figure 12a). The initial roll-up process is found to correspond to 1200 or 1800 Hz. The peak at 600 Hz indicates a pairing of two vortices emitted at 1200 Hz. Moving downstream, peaks corresponding to pairing of two (900 Hz), three (600 Hz) or four (450 Hz) vortices emitted at 1800 Hz occur. In fact, the pairing of vortices is directly related to the development of the subharmonics.[32] Also, the pairing mechanism constitutes one of the most striking features in the mixing layer dynamics.[33,34] Moreover, the peak at 750 Hz corresponds to the first acoustic mode of the cavity between the second segment and the throat.

A full analysis of this case is in progress. Also, in the future a denser mesh will be used to show the mesh effect and provide a more comprehensive look at the flow.

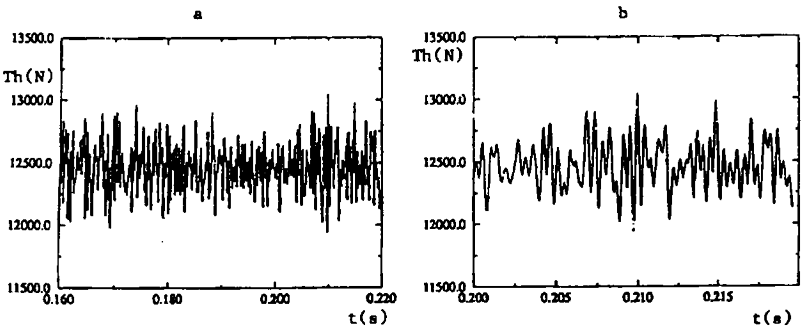

Figure 11. Time history of thrust for case III: a, complete history; b, 'zoom-in' ensemble

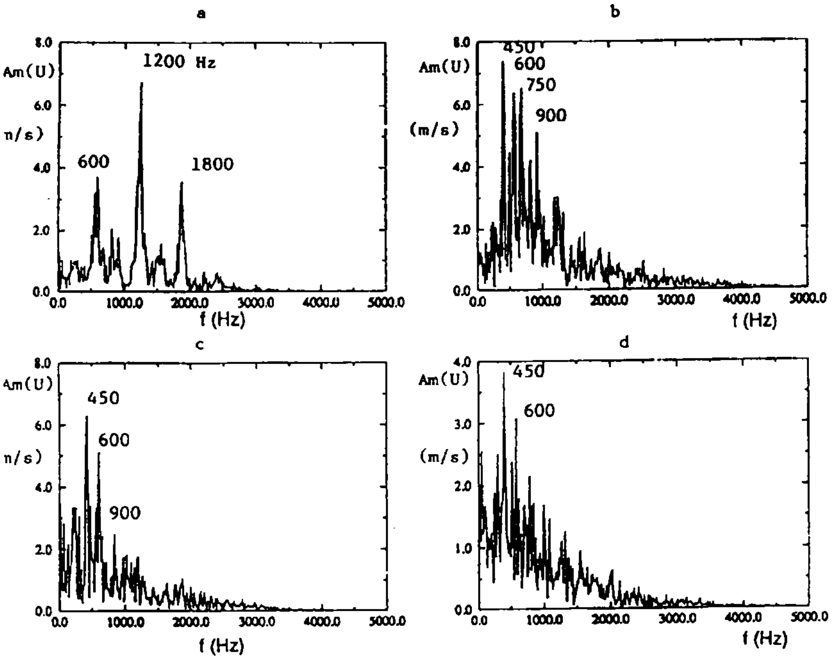

Figure 12. Spectra of U-component in mixing layer for case III: a, $x/L=0{\cdot}575$, $r/L=0{\cdot}025$; b, $x/L=0{\cdot}63$, $r/L=0{\cdot}025$; c, $x/L=0{\cdot}745$, $r/L=0{\cdot}025$; d, $x/L=0{\cdot}86$, $r/L=0{\cdot}026$

4. CONCLUSIONS

The present study has been devoted to the simulation of an acoustic boundary layer and the vortex-shedding mechanism in a rocket motor. It has shown the feasibility of the simulation of these physical mechanisms. It has also shown how to optimize the method selected to better simulate the unsteady flow behaviour and the wave acoustic propagation.

The implicit version can be used to simulate the unsteady character only with low CFL numbers ($\leqslant 50$). With increasing CFL number an increasing damping of unsteady fluctuations appears and the acoustic wave can be modified. Also, if the CFL number is too large, no unsteadiness can be predicted. With the explicit version of the code it is possible to fully predict the unsteady flow. The explicit version can be used with or without the flux-splitting technique. With this option the scheme is stable but more dissipative and introduces a damping effect in the unsteadiness. Without this technique it was possible to correctly predict the unsteady character. For this case the flux-splitting technique is only necessary for the transient period (initial phase).

The first case computed involves an acoustic boundary layer that develops above the burning propellant of a solid rocket motor. The results concern a standing acoustic wave regime that is established through pressure forcing at a given frequency. The second test case concerns the capture of the vortex-shedding phenomenon in a 2D planar configuration. The vortex shedding is predicted and its frequency corresponds to the second axial mode frequency. The last configuration studied is more representative of the solid rocket motor. In this case the vortex-shedding mechanism is correctly predicted. This mechanism is not monochromatic as in the previous case. The spectra displayed more than one frequency and its harmonics. The pairing mechanism is detected. This case will be fully analysed in the future.

ACKNOWLEDGEMENTS

This work has been supported by CNES/ONERA contract 89/3640. I wish to express special thanks to Mr. F. Vuillot of ONERA for his help and to Dr. H. C. Boisson for valuable comments. The author thanks also Dr. J. B. Cazalbou, Professor P. Chassaing and Professor H. Ha Minh.

APPENDIX: NOMENCLATURE

a	speed of sound
A	Jacobian matrix of F
$Am(\ )$	amplitude
B	Jacobian matrix of G
E	total energy
f	frequency
F	flux in axial direction
G	flux in transverse direction
h	chamber half-height
H	vector of source terms
l	length
L	chamber length
$\dot{m}$	injection mass flow rate, $(\rho v)_{\mathrm{inj}}$
M	Mach number
P	pressure
Pr	Prandtl number
r	transverse co-ordinate
R	perfect gas constant
S	Strouhal number
t	time
T	temperature
T_{f}	flame temperature
T_{i}	injection stagnation temperature
Th	thrust
U	axial or longitudinal velocity
V	transverse velocity
V_{c}	propellant burning rate
W	vector of conservative flow variables
x	axial or longitudinal co-ordinate
Greek letters	
α	coefficient of pressure forcing
γ	ratio of specific heats
λ	thermal conductivity
μ	dynamic viscosity
ρ	density
ρ_{p}	propellant density
$\sigma_{xx}, \sigma_{xr}, \sigma_{rx}, \sigma_{rr}, \sigma_{\theta\theta}$	strain tensor
$\Phi(\ )$	phase angle relative to head-end pressure

REFERENCES

1. G. A. Flandro, 'Vortex driving mechanism in oscillatory rocket flows', *J. Propuls. Power*, **3**, 206–214 (1986).
2. R. S. Brown, R. Dunlap, S. W. Young and R. C. Waugh, 'Vortex shedding as a source of acoustic energy in segmented solid rocket', *J. Spacecraft*, **8**, 312-319 (1981).
3. L. K. Issacson and A. G. Marshall, 'Acoustic oscillations in internal cavity flows: nonlinear resonant interactions', *AIAA J.*, **20**, 152–154 (1982).
4. F. Vuillot and P. Kuentzmann, 'Flow turning and admittance correction: an experimental comparison', *J. Propuls. Power*, **2**, 345–353 (1986).
5. W. K. Van Moorhen, 'Flow turning in solid-propellant rocket combustion analyses', *AIAA J.*, **20**, 1420–1425 (1982).
6. L. L. Narrayanaswami, B. T. Zinn and B. R. Daniel, 'Experimental investigation of characteristics of solid-propellant, velocity-coupled response functions', *AIAA J.*, **25**, 584–591 (1987).
7. A. Flatau, 'Vortex driven sound in a cylindrical cavity', *Ph.D. Thesis*, University of Utah, 1990.
8. G. A. Flandro and H. R. Jacobs, 'Vortex generated sound in cavities', *AIAA Paper 73-1014*, 1973.
9. F. E. C. Culick and K. Magiawala, 'Excitation of acoustic modes in a chamber by vortex shedding', *J. Sound and Vibr.*, **64**, 455–457 (1979).
10. H. Nomoto and F. E. C. Culick, 'An experimental investigation of pure tone generation by vortex shedding in duct', *J. Sound Vibr.*, **84**, 247-252 (1982).
11. W.-H. Jou and S. Menon, 'Simulation of ramjet combustor flow fields, Part II—Origin of pressure oscillations', *AIAA Paper 87-1422*, 1987.
12. R. Dunlap and R. S. Brown, 'Exploratory experiment on acoustic oscillations driven by periodic vortex shedding', *AIAA J.*, **19**, 408–409 (1981).
13. R. S. Brown, A. M. Blackner, P. G. Willoughby and R. Dunlap, 'Coupling between acoustic velocity oscillations and solid-propellant combustion', *J. Propuls. Power*, **2**, 428–437 (1986).
14. F. Vuillot, 'Acoustic mode determination in solid rocket motor stability analysis', *J. Propuls. Power*, **3**, 381-384 (1987).
15. W.-H. Jou and S. Menon, 'A mechanism of the acoustic–vortex interaction in a ramjet dump combustor', *AIAA Paper 86-1884*, 1986.
16. K. Kailasanath, J. H. Gardner, J. P. Boris and E. S. Oran, 'Acoustic–vortex interaction and low frequency oscillations in axisymmetric combustors', *AIAA Paper 87-0165*, 1987.
17. S. Menon and W.-H. Jou, 'Numerical simulation of oscillatory cold flows in an axisymmetric ramjet combustor', *J. Propuls. Power*, **6**, 525-534 (1990).
18. S. Menon and W.-H. Jou, 'Large-eddy simulation of combustion instability in ramjet combustor', *AIAA Paper 90-0267*, 1990.
19. F. Vuillot and G. Avalon, 'Acoustic–mean flow interaction in solid rocket motors using Navier–Stokes equations', *Proc. AIAA/ASEE/ASME/SAE 24th Joint Propulsion Conf. Exhib.*, Boston, MA, AiAA Paper 88-2940, July 1988.
20. N. Lupoglazoff and F. Vuillot, 'Numerical simulation of vortex shedding phenomenon in 2D test case solid rocket motors', *AIAA Paper 92-0776*, 1992.
21. J. D. Baum and J. N. Levine, 'A critical study of numerical methods for the solution of nonlinear hyperbolic equations for resonance systems', *J. Comput. Phys.*, **58**, 1–28 (1985).
22. R. W. MacCormack, 'A numerical method for solving the equations of compressible viscous flow', *AIAA Paper 81-0110*, 1981.
23. R. W. MacCormack, 'Current status of numerical solutions of the Navier–Stokes equations', *AIAA Paper 85-0032*, 1985.
24. J. L. Steger and R. F. Warming, 'Flux vector splitting of the inviscid gas dynamics equations with application to finite difference method', *J. Comput. Phys.*, **40**, 283 (1982).
25. A Kourta and H. Ha Minh, 'CAS TEST CO: couches limites acoustiques', *Contrat CNES–ONERA* 89/3640, 1991.
26. F. E. Culick, 'Rotational axisymmetric mean flow and damping of acoustic wave in a solid propellant rocket;, *AIAA J.*, **4**, 1462-1464 (1966).
27. R. Dunlap, P. G. Willoughby and R. W. Hermsen, 'Flowfield in the combustion chamber of a solid propellant rocket motor', *AIAA J.*, **12**, 1440–1442 (1974).
28. G. A. Flandro, 'Solid propellant acoustic admittance corrections', *J. Sound Vibr.*, **36**, 297–312 (1974).
29. F. Godfroy and P. Y. Tissier, 'Simulation of unsteady flows inside solid propellant rocket motors', *Colloq. CNES–ONERA*, vol. 9, Paris, December 1992.
30. A. Kourta and H. Ha Minh, 'Phénomène de détachement tourbillonnaire dans un moteur à propergol solide', *Contrat CNES–ONERA 89/3640*, 1992.
31. N. Lupoglazoff and F. Vuillot, 'Comparison between firing tests and numerical simulation of vortex shedding in 2-D test solid motor', *AIAA Paper 93-3066*, 1993.
32. C. M. Ho and P. Huerre, 'Perturbed free shear layers', *Annu. Rev. Fluid Mech.*, **16**, 365–424 (1984).
33. A. Kourta, M. Braza, P. Chassaing and H. Ha Minh, 'Numerical analysis of a natural and excited two-dimensional mixing layer', *AIAA J.*, **25**, 279-286 (1987).
34. A. Kourta, H. C. Boisson, P. Chassaing and H. Ha Minh, 'Nonliner interaction and transition to turbulence in the wake of a circular cylinder', *J. Fluid Mech.*, **181**, 141–161 (1987).